2017

Design of Electrode Arrays for 3D Capacitance Tomography in Planar Domains

S Taylor

Taylor, S, "Design of Electrode Arrays for 3D Capacitance Tomography in Planar Domains" (2017). *CTRC Research Publications.* Paper 312.
http://dx.doi.org/10.1016/j.ijheatmasstransfer.2016.10.106f

Design of electrode arrays for 3D capacitance tomography in a planar domain

Stephen H. Taylor[a,b]
Suresh V. Garimella[a,1]

[a]Cooling Technologies Research Center, an NSF I/UCRC, School of Mechanical Engineering, Purdue University, West Lafayette, IN 47907 USA.

[b]United Technologies Research Center, 411 Silver Lane, East Hartford, CT 06118 USA.

Abstract

Electrode design is investigated for electrical capacitance tomography on a 1 mm-thick 3D planar domain. Arrays of square electrodes are located on both sides of the domain, which is filled with dielectric material. Anomalies of interest are voids in the material with low dielectric constant. Simulated tomography is conducted with various electrode patterns over a range of electrode sizes in order to compare performance. The high-aspect-ratio domain requires a large finite element mesh for simulating electric fields and for defining spatial sensitivity responses of electrode pairs. Compared to the canonical 2D pipe cross-section problem, this high-aspect-ratio system requires solving the reconstruction problem on a much larger mesh and is more severely underdetermined. An efficient methodology for characterizing the sensitivity responses of various electrode pairs is developed. An image reconstruction algorithm creates binary images by sequentially composing a list of occupied cells, conditioned with a cell-to-cell energy formulation. A parametric study of four candidate electrode patterns is conducted using electrode sizes between 0.8 mm and 1.6 mm, in which each potential design is used to perform tomographic reconstruction of 100 images. A new image-error metric is proposed, which is used to evaluate each electrode design. It is found that an electrode matrix pattern on each substrate, with the patterns offset, results in lower mean image error than other candidate patterns.

Keywords: image reconstruction, 3D capacitance tomography, optimized design, electrode design

1. Corresponding author, sureshg@purdue.edu.

1. Introduction

In capacitance tomography, electrodes around a domain boundary are used to obtain capacitance measurements containing information regarding the permittivity distribution inside the domain. A common domain considered is the cross-section of a pipe [1, 2, 3, 4, 5], although other domains that have also been investigated include a cube [6], square cross-section [7, 8], volume near a single free wall [9], and a human chest cavity [10].

Electrical Capacitance Tomography (ECT) is conducted with electrodes on the boundary of a domain of interest containing some unknown distribution of dielectric materials. A total of M measurements (max $K(K\text{-}1)/2$) is taken, which must be used to reconstruct the permittivity values in N image cells, with $N >> M$. The choice of electrode number K, for a given system is a critical design consideration for real systems experiencing finite measurement noise. If K is large, the greater number of electrodes can capture more information regarding the permittivity distribution, but also require comparatively smaller-sized electrodes, with lower nominal capacitance values, and worse signal-to-noise ratio. On the other hand, as electrode number decreases, the resolution in capturing information is lost. Thus, for a very large number of electrodes bordering the domain, most of the information contained in the measurements is lost to noise, while at the limit of only two electrodes in a system, only a bulk void fraction may be obtained. In prior work, the authors have demonstrated that the mean L_2 norm image error over a set of test images has a theoretical minimum with respect to electrode number for a 2D square domain which depends on the magnitude of signal noise [8].

Capacitance-sensing of small-scale, planar domains has recently been investigated [11, 12], with the objective of imaging defects in thin layers of dielectric materials, such as pads of thermal interface material (TIM). Such a system may be used to image internal voids in coupons of dielectric materials, or bubbles in dielectric fluid flows. Characterization of high-aspect-ratio domains may be accomplished via an orthogonal mesh configuration, in which perpendicular rakes on opposing substrates are used to obtain a tessellated set of local void fractions across the footprint of the domain [11, 13, 14]. An orthogonal

mesh sensor only provides 2D information. Full 3D tomography of high-aspect-ratio domains presents significant challenges in regards to computation and physical design. In earlier work, the authors have shown that in a high-aspect-ratio domain (15:15:1), a matrix of electrodes on one side of the domain and a single large electrode on the opposing side provide sufficient tomographic data to reconstruct rudimentary 3D void features [15] in a dielectric thermal pad. In the present work, the physical design of a capacitance tomography system is investigated for conducting 3D tomography on the planar domain illustrated in Figure 1a. The material under test (MUT) is interrogated by arrays of square electrodes borne by confining substrates as illustrated in Figure 1b. Different electrode sizes and placement patterns are investigated to determine their influence on the fidelity of the 3D reconstruction.

2. System modeling

2.1 Simulation model

The system considered (illustrated in Figure 1b) is composed of a 13.4 mm × 13.4 mm × 1 mm dielectric MUT sandwiched between two confining substrates, each containing flush-mounted electrodes that face the MUT. The system is simulated on a rectilinear grid of 134 × 134 × 16 mesh cells. The *x*-*y* aspect of the mesh is a regular grid with cell dimensions $\Delta x = \Delta y = 0.1$ mm. In the *z* aspect of the mesh, $\Delta z = 0.1$ mm inside the MUT volume, $\Delta z = 0.025$ mm for the substrate depth containing electrically conductive cells comprising electrodes, and $\Delta z \approx 0.1$ mm for two cells of further depth into each substrate.

The arrangement of the electrodes on the substrates is defined by four geometric parameters, which are illustrated in Figure 2. The parameters are the electrode size *w*, an electrode row offset in a brick pattern *b*, and pattern staggering between the two substrates g_1 and g_2. The lateral gap between electrodes on a substrate *t*, is held constant at 0.2 mm, which allows for two mesh cells to reside in this space between electrodes. For a real system, the minimum electrode spacing would be selected based on the ability of the capacitance transducer to withstand large capacitance-to-ground differences.

The governing equation for electric potential is the divergence of electric displacement field,

$$\nabla \cdot (\varepsilon \nabla \varphi) = 0 . \tag{1}$$

Cells comprising electrodes are held at constant potential during simulation. A sender electrode is designated at a high constant potential $\varphi = V_{high}$, while all other electrodes are assigned a low potential $\varphi = V_{low}$. Outer boundaries of the domain have a zero-flux condition imposed. The values of dielectric constant $\varepsilon_r = \varepsilon/\varepsilon_o$ used in the model are $\varepsilon_{r,\,\mathrm{MUT}} = 5$ for the nominal MUT, $\varepsilon_{r,\,\mathrm{void}} = 1$ for void cavities, and $\varepsilon_{r,\mathrm{sub}} = 3$ for the substrates. After solving for the distribution of electric potential throughout the field, the capacitance between the sender electrode *i*, and any other electrode *j*, is obtained by integrating electric displacement flux over the entire surface of electrode *j* as

$$C_{i,j} = \frac{1}{V_i - V_j} \int_{elec\ j} \varepsilon \nabla \varphi \cdot \mathrm{n} \, \mathrm{ds} . \tag{2}$$

Calibration capacitance values C_{high} and C_{low} are calculated using Equation 2 with $\varepsilon(x,y,z) = \varepsilon_{high}$ or $\varepsilon(x,y,z) = \varepsilon_{low}$ inside the MUT volume, respectively. It is noted that capacitance C of electrode pair *i-j* is always independent of the sender-receiver roles although the solutions for $\varphi(x,y,z)$ are different. By considering all possible receiver electrodes *j*, a single solution for $\varphi(x,y,z)$ may be used to represent K-1 individual electrode pairs, and the entire combinatorial set of $K(K\text{-}1)$ electrode pairs may be modeled in K simulations. It is convenient to represent the capacitance measurements from M usable electrode pairs as a vector of referenced values $\boldsymbol{\mu}$, where

$$\mu_m = \left(C - C_{low}\right)_{i,j} . \tag{3}$$

Thus, $\boldsymbol{\mu} = \mathbf{0}$ corresponds to a completely voided region in place of the MUT, and $\mu_m = (C_{high} - C_{low})_{i,j}$ corresponds to a MUT with no void content.

It is generally observed that only pairs of electrodes in close proximity provide sufficient signal to incorporate into the measurement vector $\boldsymbol{\mu}$. Given that the goal of the present design investigation is to optimize the electrode pattern without edge effects, a subset of electrodes is defined using a disk of radius R in the center of the system. These electrodes serve as active electrodes for the study. For a parametric study, the parameter R must be large enough to capture a representative portion of the electrode pattern,

but small enough to limit undue computational expense, which may be accomplished with $R \geq 2w$. The computational savings is gained by only considering active electrodes for sender/receiver roles. A smaller disk of radius r is also identified, wherein phantom objects may be placed for conducting simulated tomography. An example electrode geometry with these radial limits shown is illustrated in Figure 3 with active electrodes in blue. Through preliminary studies, appropriate values of r and R were established as 1.25 mm and 3.0 mm, respectively when void size is comparable to the MUT thickness.

2.2 Sensitivity distributions

Recovery of the permittivity distribution throughout the domain based on a series of M capacitance measurements presents an inverse problem. This problem is linearized by constructing an approximation of the change $\Delta\mu_m$ expected in the m^{th} capacitance measurement due to a normalized permittivity change $\Delta\varepsilon_n$ in a given cell n. The description of this sensitivity is recorded in $S_{m,n}$, satisfying $\Delta\mu_m = S_{m,n}\,\Delta\varepsilon_n$. Because values of ε_n take on values between ε_{low} and ε_{high}, it is convenient to define a normalized permittivity vector $\boldsymbol{\xi}$, where

$$\xi_n = \left(\frac{\varepsilon - \varepsilon_{void}}{\varepsilon_{MUT} - \varepsilon_{void}} \right)_n . \tag{4}$$

The linear approximation of the system is given by

$$\mathbf{S}\boldsymbol{\xi} = \boldsymbol{\mu} . \tag{5}$$

For 2D problems, appropriate values for the sensitivity matrix **S**, are commonly generated by simulating all measurements for N cases, where mesh cell n in the n^{th} case is changed from a constant background permittivity value across all other cells. This approach is infeasible for large 3D meshes. In large systems, generation of sensitivity distributions has been done successfully using electric field lines [15, 16], or from the solutions for electric field. The latter approach is employed in this work. The derivation of Lucas *et al*. [17] is used for approximating the change in capacitance of an electrode pair due to a local change in permittivity at all locations in the dielectric media, which is independent of the sender-receiver roles, and is termed the *sensitivity distribution* of the pair. Two simulation solutions for

$\varphi(x,y,z)$ are used to find the sensitivity distribution for an *i*-*j* pair. First, $\varphi(x,y,z)$ is found with electrode *i* at raised potential providing discrete electric field $\overset{\mathbf{v}}{\mathrm{E}}_{i,j}(x,y,z)$; then, $\varphi(x,y,z)$ is found with electrode *j* acting as sender at raised potential, providing electric field $\overset{\mathbf{v}}{\mathrm{E}}_{j,i}(x,y,z)$. The referenced capacitance measurements for an image of known relative permittivities $\boldsymbol{\varepsilon}$, may then be approximated as

$$\mu_m \cong \sum_{n=1}^{N} \left(\varepsilon_n - \varepsilon_{low}\right)\left(\overset{\mathbf{v}}{\mathrm{E}}_{i,j} \cdot \overset{\mathbf{v}}{\mathrm{E}}_{j,i}\right)_n v_n \,, \tag{6}$$

where v_n is the volume of cell *n*.

As mentioned previously, due to the high aspect ratio of the domain, only measurements using electrodes which are in close proximity to one another yield signals above a reasonable noise level. Uncertainty due to noise is termed *u*. Sensitivity distributions with values less than twice the noise level ($\mu_m < 2u$) are removed from **S**, and the corresponding measurement μ_m is removed from $\boldsymbol{\mu}$. Row *m* in **S** represents the sensitivity distribution for the m^{th} measurement. Within the distribution, the sensitivity of cell *n* is given by

$$\mathrm{S}_{m,n} = \beta_m \left(\varepsilon_{high} - \varepsilon_{low}\right)\left(\overset{\mathbf{v}}{\mathrm{E}}_{i,j} \cdot \overset{\mathbf{v}}{\mathrm{E}}_{j,i}\right)_n v_n, \text{ where } \beta_m = \frac{\left(C_{high}\right)_m - \left(C_{low}\right)_m}{\left(\varepsilon_{high} - \varepsilon_{low}\right)\sum_{n=1}^{N}\left(\overset{\mathbf{v}}{\mathrm{E}}_{i,j} \cdot \overset{\mathbf{v}}{\mathrm{E}}_{j,i}\right)_n v_n}. \tag{7}$$

The vector $\boldsymbol{\beta}$ is a set of scaling factors ensuring that the linearized prediction (Equation 5) is equivalent to the simulated values (Equation 3) for the case where the MUT contains no void content ($\boldsymbol{\xi} = \mathbf{1}$), as described in detail in [8]. The puissant cells of a typical sensitivity distribution are shown in Figure 4, with locations of the cells shown in Figure 4a, and an illustration of the same cells colored according to relative sensitivity in Figure 4b. The distribution may be described as a tunnel of positive sensitivity within a sheath of weaker negative sensitivity. The image reconstruction problem is defined as recovery of normalized permittivity $\boldsymbol{\xi}$, using Equation 5, given **S** and $\boldsymbol{\mu}$.

2.3 Image reconstruction technique

Many image reconstruction techniques have been investigated for ECT. The least expensive method is linear back projection (LBP), which is a popular industrial choice when images need to be captured and displayed in real time. Another choice for rapid image reconstruction is Tikhonov regularization, which provides better image segmentation of objects. When using electrodes directly exposed to the MUT, Tikhonov regularization is prone to reconstructing false artifacts near electrode walls, where sensitivity is very high. Recently, a new explicit formulation for image reconstruction called sensitivity factor regularization (SFR) has been proposed, which suppresses the artifacts produced in Tikhonov regularization with comparable or better image segmentation [8].

When computation time may be devoted to reconstructing individual images, iterative algorithms are preferred. Landweber iteration is popular in the literature [3, 18, 19], and is based on a steepest descent optimization routine that generally produces much better image segmentation than explicit methods, although hundreds of iterations may be required. Other iterative algorithms include algebraic reconstruction technique (ART), simultaneous iterative reconstruction technique (SIRT), Newton methods, and iterative formulations of explicit methods [5, 7].

For a large 3D domain where two distinct phases are to be reconstructed, the authors have developed the shape-energy evolutionary algorithm (SEER) which strictly enforces a binary solution [15]. In the present work, the SEER algorithm is used. The steps of the algorithm are described herein, with a summary illustration in Figure 5. For a detailed explanation of SEER, the reader is referred to [15].

First, the algorithm is initialized using an explicit method. Although Tikhonov regularization and the SFR method are inexpensive means for providing fair results, both require a regularization parameter which must be optimized empirically for each design, which is not feasible for a parametric study of a large system. While less accurate than Tikhonov and SFR, the LBP method brings the benefits of high noise resilience and freedom from empirically chosen regularization parameters. Furthermore, the final result of the SEER algorithm is generally insensitive to minor improvements in the initialized image. The LBP method requires definition of the LBP sensitivity matrix $\mathbf{S}_{\mathrm{LBP}}$, which is a normalization of $\mathbf{S}$ such

that all columns sum to 1. The normalized measurement vector $\mu_{LBP,m} = \mu_{,m} /(C_{\text{high}} - C_{low})_m$ is also required. The initialized solution is then found as $\boldsymbol{\xi} = \mathbf{S}_{\text{LBP}}^{\text{T}} \boldsymbol{\mu}_{LBP}$. An example void cavity is shown in Figure 5a with the LBP image reconstruction shown in Figure 5b. Because reconstructions are not inherently binary, LBP images do not provide well-defined characteristics of the void, such as shape, volume, and boundaries.

After the initial LBP reconstruction, the SEER algorithm begins by using the complimentary normalized permittivity (or image) vector $\bar{\boldsymbol{\xi}} = \mathbf{1} - \boldsymbol{\xi}$. The image vector begins as $\bar{\boldsymbol{\xi}} = \mathbf{0}$, corresponding to a case where no voids exist. The image representing a void is a rendering of $\bar{\boldsymbol{\xi}}$, where cell *n* is rendered as occupied in the void cavity ($\bar{\xi}_n = 1$) and vacant outside the void ($\bar{\xi}_n = 0$). In the SEER algorithm, all cells of the current image, both occupied and vacant, are characterized by an energy value equal to the sum of squared distances to occupied cells within a local neighborhood. In this work, a radius of 0.21 mm is chosen to define the local neighborhood. Thus, cell locations that are near occupied cells have low energy. All cells are assigned a priority value equal to the reciprocal of the energy value. This may be accomplished efficiently using a $N \times N$ matrix containing the priority values. One iteration of the image is constructed by examining cells sequentially in order of priority, where cell *n* is the p^{th} priority cell, and then rendering them as occupied if they qualify. To qualify, occupation of the cell must result in a better match between the predicted measurement vector **x**, and the known measurement vector $\boldsymbol{\mu}$, in the sum of absolute discrepancies. Thus, at step *p*, where cell *n* is examined, the predicted measurement vector advances as

$$\mathbf{x}^p = \begin{cases} \mathbf{x}^{p-1} + \mathbf{S}_{\text{g}\,n} & \sum_{m=1}^{M} |\mathrm{x}^{p-1} + \mathrm{S}_{m,n} - \mu|_m < \sum_{m=1}^{M} |\mathrm{x}^{p-1} - \mu|_m \quad \textit{occupy} \\ \mathbf{x}^{p-1} & \sum_{m=1}^{M} |\mathrm{x}^{p-1} + \mathrm{S}_{m,n} - \mu|_m \geq \sum_{m=1}^{M} |\mathrm{x}^{p-1} - \mu|_m \quad \textit{do not occupy} \end{cases} . \tag{8}$$

When the image has either fulfilled the tomographic constraints within a specified tolerance or no new cells have been rendered after a predetermined large number of evaluations (stagnation), the image is complete. Figure 5c illustrates the first iteration of SEER.

The algorithm iterates by using the complete image to construct a new prioritization field, and the next iteration of the image is rebuilt beginning with a blank backdrop, $\bar{\boldsymbol{\xi}} = \mathbf{0}$. The method of constructing the prioritization field does not require a binary input image, thus allowing for the first prioritization field to be initialized using the non-binary LBP solution. Subsequently, the prioritization field is created with binary images created during iterations of SEER. Over the course of several iterations, rendered shapes in the image tend to lose small-scale features which were remnants of the sensitivity distributions themselves, and small, lone groups of cells tend to be eliminated, as evident in Figure 5d. Convergence is obtained when reconstructed images differ by less than a predetermined residual value, or when a predetermined maximum number of iterations have been performed. In this work, an image residual value of $0.05\Sigma_i[(\xi_i - \xi_{previous,i})/\xi_{previous,i}]$ is used, along with a maximum iteration number of 15.

3. Design study

3.1 Design candidates

Many potential electrode patterns could be employed for conducting tomography with two planes of electrodes. The scope of this work considers four distinct patterns using arrays of square electrodes shown in Figure 6. A regular grid of square electrodes, with the electrodes on the bottom aligned with electrodes on the top, is termed an *Aligned Matrix* configuration. A regular grid of square electrodes, with the electrodes on the top offset against the electrodes on the bottom, is termed an *Offset Matrix* configuration. An array of staggered rows of electrodes, such that the electrode arrays create a brick pattern, with the electrodes on the bottom aligned with the top, is termed an *Aligned Staggered* configuration. A staggered brick pattern, with electrodes of the top substrate offset to place all interstitial intersections directly opposite a region spanned by an opposing electrode face is termed an *Offset Staggered* configuration.

Each of the electrode patterns is tested with electrode size ranging from 0.9 mm to 2.4 mm with spacing t = 0.2 mm. Where necessary, design variables calculated from the formulas shown in Figure 6 are rounded for mapping to the discrete mesh. Measurement noise is introduced into the simulated measurements by adding a vector of random values between $-u$ and u to the vector $\boldsymbol{\mu}$ for each case prior to initiating the image reconstruction routine. Entries of $\boldsymbol{\mu}$ are then thresholded such that entries that are within uncertainty u of zero (minimum value for all measurements) are reset to zero, and entries that are within uncertainty u of their respective maximum values are reset to their maximum values (see Equation 3).

3.2 Design evaluation

In order to evaluate the accuracy of image reconstructions, a quantitative measure of discrepancy between two images is required. The L_2 norm of the difference between the nominal and reconstructed image vectors may be used to calculate an error between the correct image vector $\bar{\xi}_o$, and the reconstructed image vector $\bar{\xi}_r$, as

$$E_{L2} = \frac{\left\| \bar{\xi}_o - \bar{\xi}_r \right\|}{\left\| \bar{\xi}_o \right\|}. \tag{9}$$

Although this measure of image error is often used [3, 4, 18], it treats all incorrectly rendered cells with equal weight, which does not offer a complete measure reflecting the correctness of the image useful to an application. For binary images, a new spatial image error E_S, is proposed, which is composed of error E_S^- due to false negatives (cells reconstructed as vacant but are occupied in the correct image) and E_S^+ due to false positives (cells reconstructed as occupied but are vacant in the correct image). The overall spatial image error is $E_S = E_S^- + E_S^+$, where E_S^- and E_S^+ are calculated using the following:

- *False negative error* E_S^-: For each cell corresponding to a false negative, the nearest occupied cell in the reconstructed image is determined. The square root of the distance between the two in cell lengths is calculated as spatial image error. The sum of all such errors is E_S^-.
- *False positive error* E_S^+: For each cell corresponding to a false positive, the nearest vacant cell in the reconstructed image is determined. The square root of the distance between the two in cell lengths is calculated as spatial image error. The sum of all such errors is E_S^+.

When a cell is sought and not found (*e.g.*, no nearest occupied cell exists because no cells are occupied), the spatial image error is calculated as the square root of the image width in cell lengths.

In order to illustrate the nature of the spatial image error E_S, Figure 7 shows a 2D image (Figure 7a) with several comparison images (Figure 7b-g). Each of the comparison images has been fabricated to exhibit the same L_2 norm discrepancy from the first image; these images would likely be interpreted as exhibiting varying degrees of correctness. The spatial error metric better captures a realistic image correctness where incorrectly rendered cells are weighted more heavily when they are further astray from true image features. It is noted that although both definitions of discrepancy yield zero for two identical images, their magnitudes cannot be directly compared; the parameter E_S ranges over a far wider numerical span than E_{L2}.

In this work, electrode designs are characterized by a mean expected image error $\bar{E}_S$, obtained by performing tomographic reconstructions of a large number of images for each design. It is observed that a test set of 100 images is sufficient to resolve trends and contrasts in performance between designs. Simulation of the capacitance measurements for these images for each design candidate is highly expensive. For computational simplification, the linearized forward calculation of the measurement vector is employed, $\boldsymbol{\mu} = \mathbf{S}\boldsymbol{\xi}_o$. By so doing, second-order effects (soft-field variations) are neglected at significant computational gain. Due to the large mesh size, high-fidelity solutions for $\boldsymbol{\mu}$ are intractable for the scope of the current study. However, critical design aspects, including the underdetermined nature of

the problem and the influence of noise in measurements, are incorporated into the study. For a broad comparative study, the linearization aptly captures comparative performance. Figure 8 summarizes the process used to characterize each candidate electrode design. Selected images from the test set are shown in Figure 9. Each image contains a randomly shaped and oriented void in the shape of an ellipsoid or ellipsoid fragment. The images are generated to represent a variety of the types of void structures that might be expected in a planar domain. Voids occupy random positions within the cylindrical volume defined by radius *r*.

4 Numerical results

Selected image reconstructions are shown in Figure 10, which correspond to the selected test images shown in Figure 9. The image reconstructions shown were performed using the Aligned Matrix configuration with w = 1.2 mm.

In Figure 11, mean image error $\bar{\bar{E}}_S$, is shown for the Aligned Matrix configuration versus electrode size *w*, for several different noise levels. As electrode size decreases, more independent measurements are possible; however, the measurements also become more subject to noise. The competing effects result in an optimum electrode size for image reconstruction. The electrode sizes with observed minimum mean image error in the numerical study are indicated on the plot. The optimal electrode size is larger for higher signal noise levels, and smaller than 9 mm for the lowest noise level.

For industrial applications, computational limitations may require that electrodes be designed to be larger than the optimal size when characterizing a high-aspect-ratio domain. The results for mean image error $\bar{\bar{E}}_S$ for the four candidate electrode designs at a signal noise level of 0.5 fF are shown in Figure 12 for electrode sizes between 1.0 mm and 2.4 mm. The Offset Matrix and Offset Staggered designs perform better than the aligned designs, especially at large electrode sizes. The two offset configurations perform equally well within the resolution of this study. As electrode size decreases,

differences in performance diminish until performance is approximately the same for all the systems at w = 1 mm.

The improved performance of the offset configurations is attributed to better quality of the sensitivity distributions produced by these electrode arrangements. The number of electrode pairs providing usable capacitance measurements above the noise level after applying the methodology in Section 2.2 is given in Table 1. While up to several thousand unique electrode pairs may exist, only pairs that produced signal of twice the noise level were retained for defining the sensitivity matrix. The quality of a set of sensitivity distributions is more important than their number, as the aligned patterns generally give rise to a greater number of sensitivity distributions, but perform more poorly than the offset designs. The quality of a sensitivity distribution may be understood conceptually. When the top and bottom electrode patterns are aligned, a strong signal is produced between directly opposing electrodes, creating a "high-quality" sensitivity distribution. The signal obtained using any other electrode pair representing opposing substrates is significantly attenuated, with poorer signal-to-noise ratio. Conversely, when the Offset Matrix pattern is used, a given bottom electrode produces four different sensitivity distributions with proximate neighbors from the top substrate, each with moderately strong signal of "high quality". A similar effect is observed in the Offset Staggered configuration, although only in two opposing neighbors instead of four. The utility of the tomographic information obtained from the system improves not only with quality of the sensitivity distributions, but also with morphological diversity in the way the distributions weight individual cells. The mathematical necessity of satisfying a more diverse set of distributions strengthens the constraints on the inverse problem and improves the final result. The approach developed herein for evaluating electrode designs may be used to investigate comparative performance of the different electrode patterns as a function of signal-to-noise ratio.

5. Conclusion

The design of electrodes for performing capacitance tomography on a planar domain using electrode arrangements on each face is numerically investigated. A computationally efficient

methodology for formulating the linear model for a large 3D system is presented along with a reconstruction algorithm which always produces binary images. A new metric for spatial image error is proposed which better quantifies a realistic measure of the correctness of an image. A detailed investigation is conducted in which images were reconstructed using four candidate electrode designs at different electrode sizes. In the investigation, a means of reducing the parametric study to a tractable set of computation is demonstrated through the use of linearization in the forward problem, and the use of the SEER algorithm in the reconstruction problem. Two designs using matrix arrays of electrodes and two using staggered arrays were considered. For each array type, an aligned and an offset condition between top and bottom substrates was investigated. The results indicate that offset designs outperform the other designs when electrodes are larger than the thickness of the domain, with the benefit diminishing with decreasing electrode size. Thus, in theory, a smaller electrode density using large, staggered electrodes can provide the same performance of a greater electrode density using small, aligned electrodes. The performance curves presented in the paper provide a theoretical basis for choosing electrode designs that are best candidates for further interrogation with higher fidelity computational modeling approaches and experimental investigations..

Acknowledgements

The authors gratefully recognize financial support for this work from Cooling Technologies Research Center, a National Science Foundation Industry/University Cooperative Research Center and Purdue University, as well as technical discussions with Dr. Justin Weibel.

References

[1] T. R. McKeen and T. S. Pugsley, "The Influence of Permittivity Models on Phantom Images Obtained from Electrical Capacitance Tomography," *Measurement Science and Technology,* vol. 13, pp. 1822-1830, 2002.

[2] B. Kortschak, H. Wegleiter and B. Brandstatter, "Formulation of Cost Functionals for Different Measurement Principles in Nonlinear Capacitance Tomography," *Measurement Science and Technology,* vol. 18, no. 1, pp. 71-78, 2007.

[3] L. F. Zhang and H. X. Wang, "A New Normalization Method Based on Electrical Field Lines for Electrical Capacitance Tomography," *Measurement Science and Technology,* vol. 20, 2009.

[4] S. Teniou, M. Meribout, T. A. Hanaei, F. A. Zaabi, R. Banihashim and S. A. Ghafri, "A New Constrained Hierarchical Reconstruction Method for Electrical Capacitance Tomography," *Flow Measurement and Instrumentation,* vol. 23, pp. 66-75, 2012.

[5] T. Loser, R. Wajman and D. Mewes, "Electrical Capacitance Tomography: Image Reconstruction Along Electrical Field Lines," *Measurement Science and Technology,* vol. 12, pp. 1083-1091, 2001.

[6] S. Ren, Y. Xu, C. Tan and F. Dong, "Reconstructing the Geometric Configuration of Three Dimensional Interface using Electrical Capacitance Tomography," *International Journal for Numerical Methods in Engineering,* vol. 96, pp. 628-644, 2013.

[7] W. Q. Yang and L. Peng, "Image Reconstruction Algorithms for Electrical Capacitance Tomography," *Measurement Science and Technology,* vol. 14, pp. R1-R13, 2003.

[8] S. H. Taylor and S. V. Garimella, "An Explicit Regularization Method for Electrical Capacitance Tomography," *Flow Measurement and Instrumentation,* p. (in review), 2015.

[9] J. L. Mueller, D. Isaacson and J. C. Newell, "A Reconstruction Algorithm for Electrical Impedance Tomography Data Collected on Rectangular Electrode Arrays," *IEEE Transactions on Biomedical Engineering,* vol. 46, no. 11, pp. 1379-1386, 1999.

[10] P. Rahmati, M. Soleimani, S. Pulletz, I. Frerichs and A. Adler, "Level-set-based reconstruction algorithm for EIT lung images: first clinical results," *Physiological Measurement,* vol. 33, pp. 739-750, 2012.

[11] S. H. Taylor and S. V. Garimella, "Near-Field Focusing Sensor for Characterization of Void Content in Thin Dielectric Layers," *Measurement Science and Technology,* vol. 26, no. 1, p. 015601, 2015.

[12] S. H. Taylor and S. V. Garimella, "Capacitive Sensing of Local Bond Layer Thickness and Coverage in Thermal Interface Materials," *International Journal of Heat and Mass Transfer,* vol. 97, pp. 26-31, 2016.

[13] M. J. Da Silva and U. Hampel, "A Field-Focusing Imaging Sensor for Fast Visualization of Multiphase Flows," *Measurement Science and Technology,* vol. 20, 2009.

[14] Z. Cui, H. Wang, Z. Chen and W. Yang, "Image Reconstruction for Field-Focusing Capacitance Imaging," *Measurement Science and Technology,* vol. 22, 2011.

[15] S. H. Taylor and S. V. Garimella, "Shape-energy evolutionary reconstruction algorithm for electrical capacitance tomography in a high-aspect-ratio domain," *Sensors and Actuators A: Physical,* p. (in review), 2015.

[16] R. Wajman and R. Banasiak, "Tunnel-Based Method of Sensitivity Matrix Calculation for 3D-ECT Imaging," *Sensor Review,* vol. 34, no. 3, pp. 273-283, 2014.

[17] J. Lucas, S. Hole and C. Batis, "Simple and Direct Calculation of Capacititve Sensor Sensitivity Map," *International Journal for Computation and Mathematics in Electrical and Electronic Engineering (COMPEL),* vol. 27, no. 1, pp. 307-318, 2008.

[18] Y. Yang and L. Peng, "A Configurable Electrical Capacitance Tomography System Using a Combining Electrode Strategy," *Measurement Science and Technology,* vol. 24, 2013.

[19] A. M. Olmos, M. A. Carvajal, D. P. Morales, A. Garcia and A. J. Palma, "Development of an Electrical Capacitance Tomography System using Four Rotating Electrodes," *Sensors and Actuators A: Physical,* vol. 148, pp. 366-375, 2008.

List of Tables

Table 1. Number of electrode pairs providing usable capacitance measurements for candidate electrode designs at a noise level of u = 0.5 fF.

w (mm)	Aligned Matrix	Offset Matrix	Aligned Staggered	Offset Staggered
1.0	343	261	284	301
1.2	287	207	218	216
1.4	197	156	161	162
1.6	171	125	130	122
1.8	145	111	126	107
2.0	128	94	108	88
2.2	102	75	95	81
2.4	89	66	73	81

List of Figures

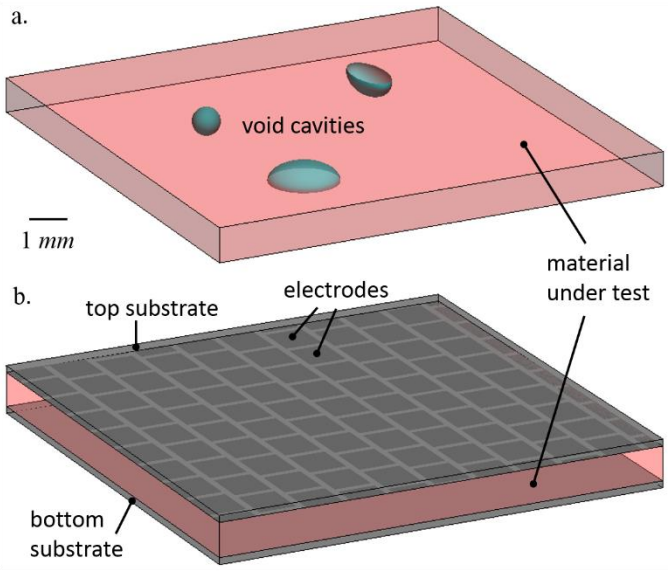

Figure 1. Illustration of the tomography system. (a) A planar coupon of material (transparent) contains void cavities. (b) The material is interrogated by two substrates bearing electrodes embedded flush with the substrate surfaces contacting the material.

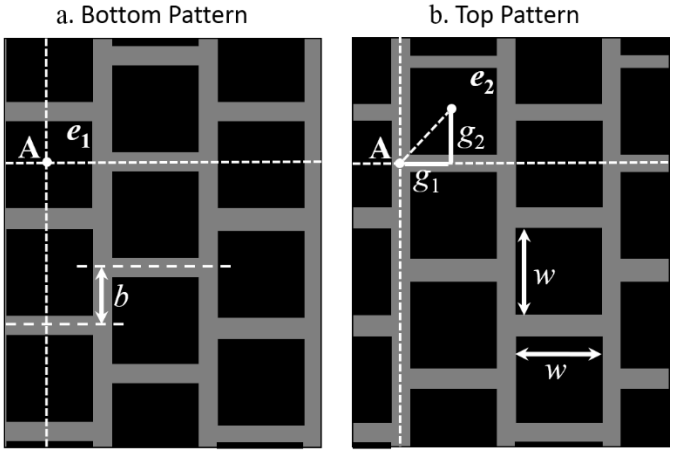

Figure 2. Parameters defining electrode patterns on the (a) bottom and (b) top substrates. A given electrode e_1 at *x-y* location A on the bottom substrate is offset from nearby electrode e_2 on the top substrate by a vector (g_1, g_2). The patterns extend over the entirety of the substrate surfaces facing the dielectric material.

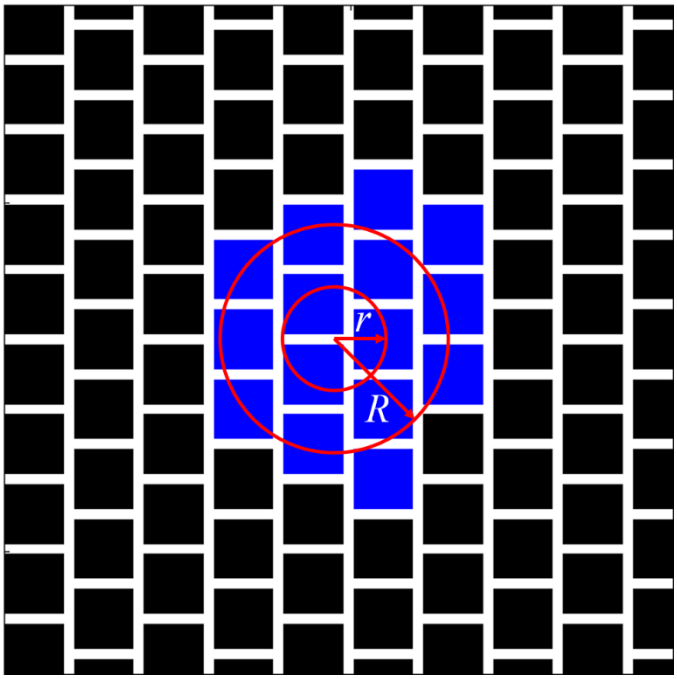

Figure 3. Active electrodes (blue) are chosen by including electrodes with any part within a radius *R*. Simulated void structures are placed within radius *r*.

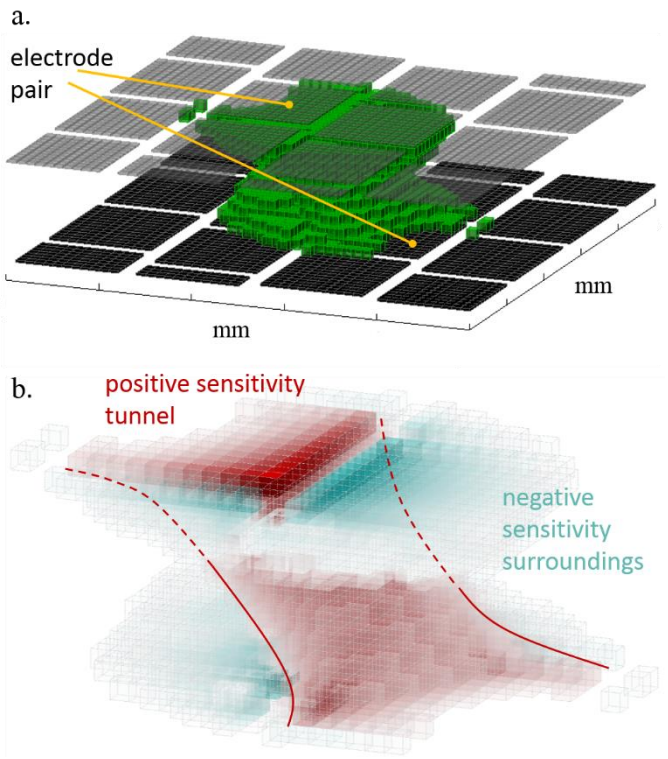

Figure 4. (a) View of select cells of a sensitivity distribution. (b) Cells of the distribution are colored red and turquoise to indicate positive and negative sensitivity, respectively, and shown with transparency reflecting sensitivity magnitude (less sensitive is more transparent).

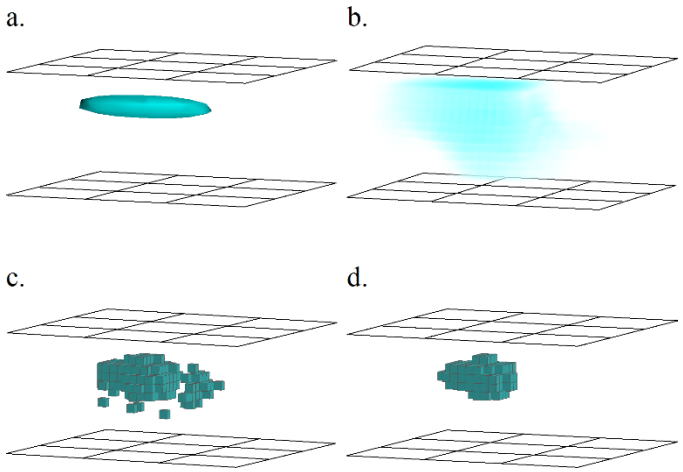

Figure 5. Image reconstruction with the SEER algorithm using the Offset Staggered design discussed in Section 3.1 with w = 1.6 mm without measurement noise. (a) True image of void cavity to be reconstructed. (b) The initialization with the LBP method. (c) Iteration 1 of the algorithm. (d) Final reconstructed image. Gridlines indicate units of mm.

Configuration	Parameters	Diagram
Aligned Matrix	$b = 0$ $g_1 = 0$ $g_2 = 0$	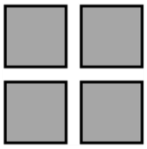
Offset Matrix	$b = 0$ $g_1 = (w+t)/2$ $g_2 = (w+t)/2$	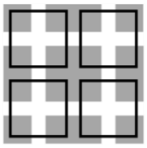
Aligned Staggered	$b = (w+t)/2$ $g_1 = 0$ $g_2 = 0$	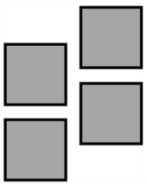
Offset Staggered	$b = (w+t)/2$ $g_1 = (w+t)/2$ $g_2 = (w+t)/4$	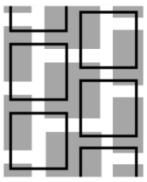

Figure 6. Electrode configuration patterns tested in the parametric study. Gray squares represent bottom electrodes and black outlines represent top electrodes.

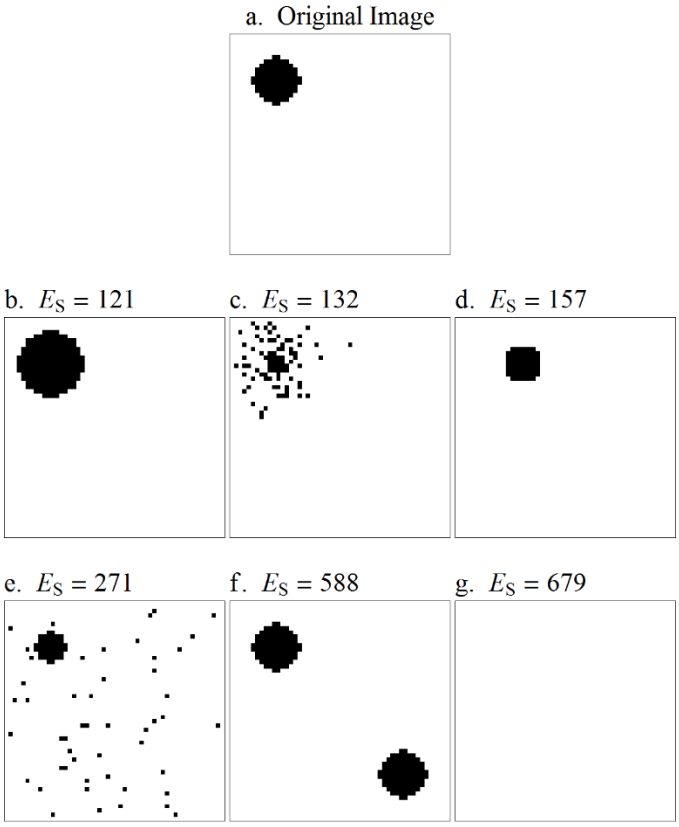

Figure 7. Spatial image error E_S for six comparison images with respect to the original. All images exhibit L_2 image error of $E_{L2} = 1$. (Images do not represent tomographic reconstructions).

Input: w, b, g_1, g_2

Characterize Design Point

1. Define electrode geometry.
2. Identify K active electrodes.
3. High permittivity calibration.
   a. Set $\varepsilon(x,y,z) = \varepsilon_{\mathrm{MUT}}$.
   b. Simulate K electric fields.
   c. Obtain C_{high} for M pairs (Eq. 2).
   d. Obtain $\vec{\mathbf{E}}$ for M pairs.
4. Low permittivity calibration.
   a. Set $\varepsilon(x,y,z) = \varepsilon_{void}$.
   b. Simulate K electric fields.
   c. Obtain C_{low} for M pairs (Eq. 2).
5. Define $\mathbf{S}$ (see Section 2.2).

Evaluate Test Images

Loop: For j from 1 to 100,
   a. Obtain vector $\boldsymbol{\mu} = \mathbf{S}\boldsymbol{\xi}_o$.
   b. Reconstruct image vector $\boldsymbol{\xi}_r$ (see Section 2.3).
   c. Obtain spatial image error E_S (Eq. 9)

End Loop

Output: mean image error, $\overline{E}_S$.

Figure 8. Process summary for evaluation of a candidate electrode design.

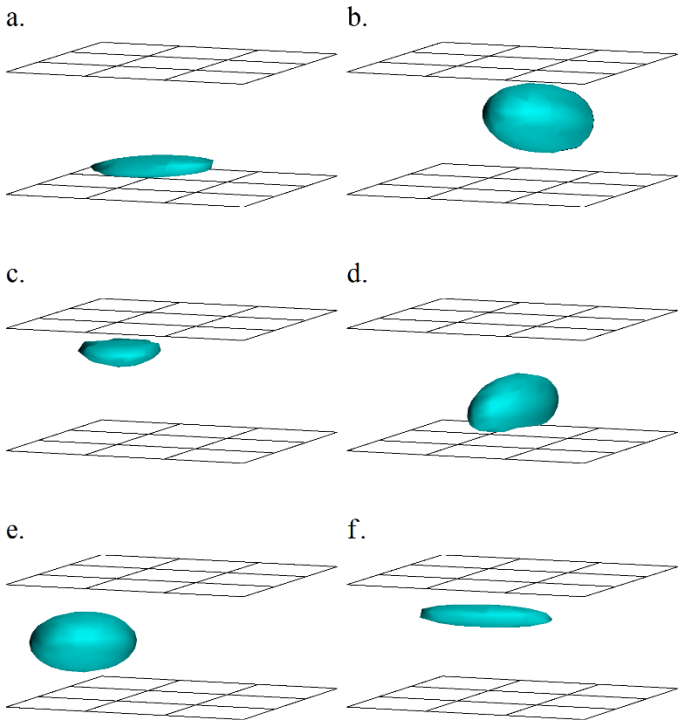

Figure 9. Selected examples from the set of 100 test images of void cavities used for evaluating candidate electrode designs. Gridlines indicate units of mm.

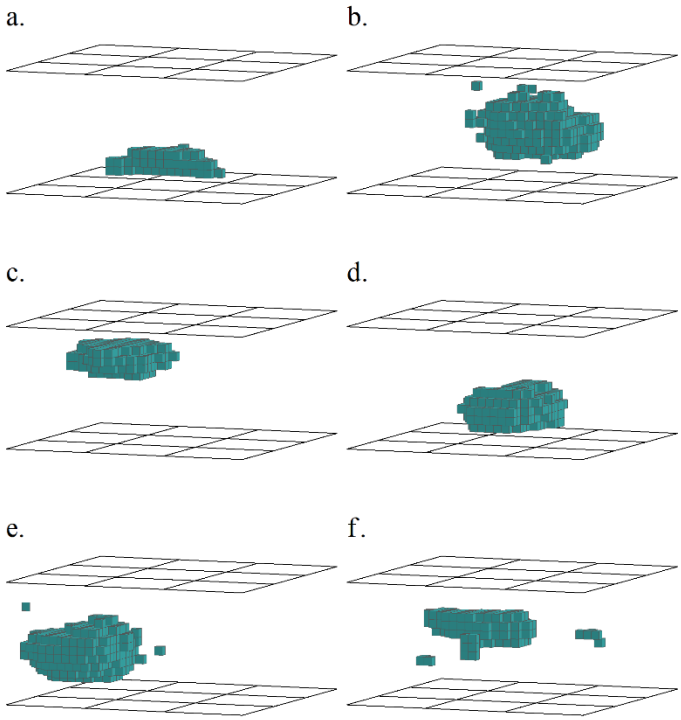

Figure 10. Reconstruction of selected void cavities shown in Fig 9 using the Aligned Matrix electrode configuration with w = 1.2 mm with measurement noise of 0.1 fF. Gridlines indicates units of mm.

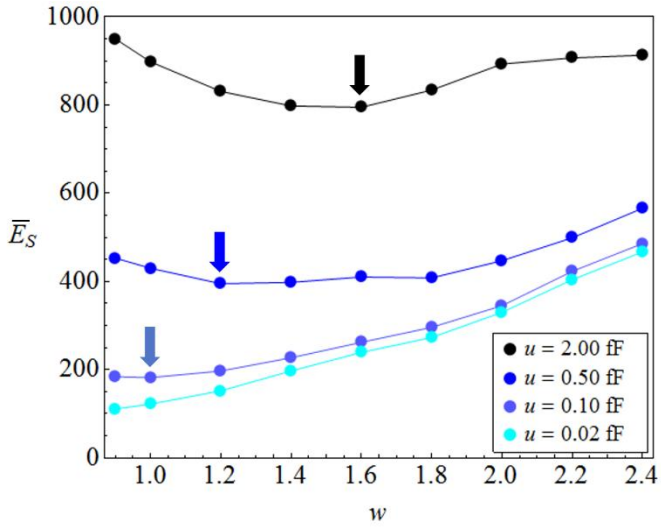

Figure 11. Mean image error, $\overline{E}_S$, over the set of 100 image reconstructions for different levels of measurement noise versus electrode size, *w*, for the Aligned Matrix configuration. Arrows indicate minima.

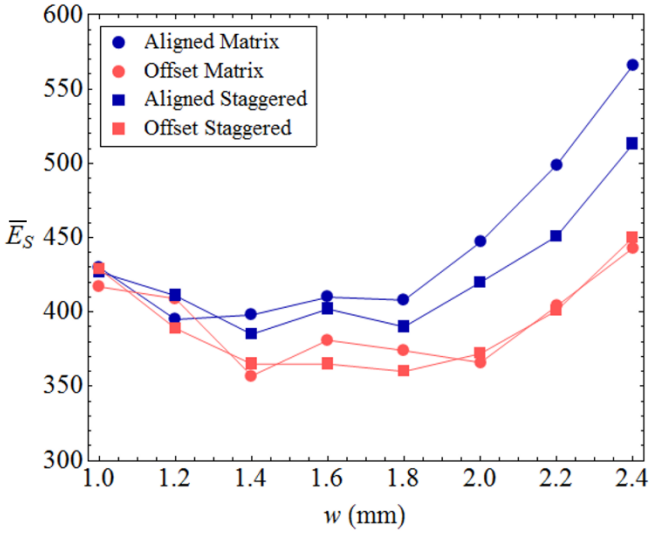

Figure 12. Mean spatial image error, $\overline{E}_S$, over the set of 100 image reconstructions for different electrode configurations versus electrode size w, at a signal noise level of 0.5 fF.